Journal of Carbon Research

MDPI

Article

Hydrogen Storage on Activated Carbons from Avocado Biomass Residues: Synthesis Route Assessment, Surface Properties and Multilayer Adsorption Modeling

Zayda V. Herrera-Cuadrado [1,2], Lizeth J. Bastidas-Solarte [1], Erwin García-Hernández [3], Adrián Bonilla-Petriciolet [1,*], Carlos J. Duran-Valle [4], Didilia I. Mendoza-Castillo [1,5], Hilda E. Reynel-Ávila [1,5], Ma. del Rosario Moreno-Virgen [1], Gloria Sandoval-Flores [6] and Sofía Alvarado-Reyna [6]

1 Instituto Tecnológico de Aguascalientes, Tecnológico Nacional de México, Aguascalientes 20256, Mexico; 25153050@aguascalientes.tecnm.mx (Z.V.H.-C.); lizeth.bastidas03@gmail.com (L.J.B.-S.); didi_men@hotmail.com (D.I.M.-C.); elizabethreynel@gmail.com (H.E.R.-Á.); ma_rosario.mv@aguascalientes.tecnm.mx (M.d.R.M.-V.)
2 Facultad de Ciencias, Escuela Superior Politécnica del Chimborazo, Riobamba 060155, Ecuador
3 Instituto Tecnológico Superior de Zacapoaxtla, Tecnológico Nacional de México, Puebla 73680, Mexico; erwin.garcia@live.itsz.edu.mx
4 Instituto del Agua, Cambio Climático y Sostenibilidad, Universidad de Extremadura, 06006 Badajoz, Spain; carlosdv@unex.es
5 Investigadoras e Investiga-dores por México, Secretaría de Ciencia, Humanidades, Tecnología e Innovación, Ciudad de México 03940, Mexico
6 Unidad Académica Multidisciplinaria Reynosa, Universidad Autónoma de Tamaulipas, Tamaulipas 87000, Mexico; gloriasfmx@yahoo.com.mx (G.S.-F.); salvarad@docentes.uat.edu.mx (S.A.-R.)
* Correspondence: petriciolet@hotmail.com; Tel.: +52-449-2576255

Abstract

This manuscript reports the preparation, surface characterization, and modeling of chars and activated carbons obtained from avocado biomass for hydrogen storage. Activated carbons were prepared from avocado biomass via the following stages: (a) pyrolysis of avocado biomass, (b) impregnation of the avocado-based char using an aqueous lithium solution, and (c) thermal activation of lithium-loaded avocado char. The synthesis conditions of char and activated carbon samples were tailored to maximize their hydrogen adsorption properties at 77 K, where the impact of both pyrolysis and activation conditions was assessed. The hydrogen storage mechanism was discussed based on computational chemistry calculations and multilayer adsorption simulation. The modelling focuses on the analysis of the saturation of activated carbon active sites via the adsorption of multiple hydrogen molecules. The results showed that the activated carbon samples displayed adsorption capacities higher than their char counterparts by 71–91% because of the proposed activation protocol. The best activated carbon obtained from avocado residues showed a maximum hydrogen adsorption capacity of 142 cm^3/g, and its storage performance can compete with other carbonaceous adsorbents reported in the literature. The hydrogen adsorption mechanism implied the formation of 2–4 layers on activated carbon surface, where physical interactions via oxygenated functionalities played a relevant role in the binding of hydrogen dimers and trimers. The results of this study contribute to the application of low-cost activated carbons from residual biomass as a storage medium in the green hydrogen supply chain.

Keywords: carbonaceous porous materials; energy transition; computational chemistry

Academic Editor: Manuel Fernando Ribeiro Pereira

Received: 26 December 2025
Revised: 6 January 2026
Accepted: 8 January 2026
Published: 12 January 2026

1. Introduction

Hydrogen (H_2) is a key molecule that plays a relevant role in achieving a carbon-neutral and sustainable future of society [1,2]. H_2 is a versatile energy carrier that will help decarbonize relevant sectors, such as heavy industry and transportation [3]. It has been classified as a relevant feedstock for the operation of green energy systems and industrial processes; however, different challenges must be resolved in terms of its generation, valorization, transportation, and management to achieve the goal of a decarbonized economy [4,5]. The worldwide energy transition agenda has emphasized that consolidating and reducing the production costs of green H_2 and its corresponding storage, distribution, and end uses are paramount to achieving sustainable large-scale applications [6–8]. In this direction, several studies have highlighted the importance of developing effective storage methods for H_2 that can support its supply chain [9–11].

The assessment of porous materials for the storage of H_2 is a cornerstone to implement commercial alternatives for its separation and transportation [12–14]. Carbonaceous adsorbents can be used for H_2 adsorption [14–19]. These materials offer multifaceted separation performance that can be tailored via the synthesis conditions of the carbon phase and its surface activation [20,21]. The consolidated supply chain of activated carbon is particularly advantageous for industrial applications of effective H_2 storage systems. However, the production cost of these adsorbents must be reduced, and effective activation protocols must be developed to improve their H_2 adsorption capacities and minimize the corresponding carbon footprint.

Low-cost activated carbons for H_2 adsorption can be obtained via the valorization of a wide spectrum of biomass waste following the circular economy basis [22,23]. Residual biomass has been recognized as a renewable, eco-friendly, and abundant resource that can be utilized industrially to produce different materials, allowing for the mitigation of the environmental impacts generated by traditional and non-renewable feedstocks, including waste minimization with simultaneous production cost reduction [24]. Various biomass residues and preparation routes have been reported to produce activated carbons for H_2 adsorption [25–27]. For instance, polypodium vulgare biomass was used to obtain activated carbon via KOH activation and pyrolysis (700–900 °C), and this adsorbent was assessed for H_2 storage at different operating conditions [28]. Palimera sprout wastes were also pyrolyzed (900 °C for 2 h) and modified with KOH to obtain activated carbon for H_2 adsorption [29], while pine and beech tree residues were pyrolyzed and activated with nitric acid and lithium hydroxide to adsorb H_2 [30]. Recently, Lionetti et al. [31] prepared an activated carbon to adsorb H_2 using a walnut shell waste and a CO_2-based activation route. Despite the advances in the state-of-the-art of activated carbon synthesis for H_2 storage, gaps remain in tailoring the adsorbent separation performance using biomass residues as feedstock and understanding the adsorption mechanism.

This study focused on the analysis and characterization of H_2 adsorption properties of activated carbon obtained from avocado waste, which is an abundant biomass in Latin American countries, particularly in Mexico. Different synthesis conditions were examined to obtain activated carbon samples from this biomass and valorize their H_2 adsorption properties at 77 K, which were compared with their char counterparts (i.e., adsorbents without surface tailoring) to establish the impact of the activation conditions. The chars and activated carbons were characterized, and the H_2 adsorption mechanism was discussed based on computational chemistry calculations and multilayer statistical physics modeling. The results of this study contribute to the development of a resilient and sustainable energy system based on green H_2 using low-cost activated carbons from residual biomass as a storage medium.

https://doi.org/10.3390/c12010005

2. Materials and Methods

2.1. Preparation of Activated Carbons for H_2 Adsorption

Activated carbons were prepared from avocado biomass via the following stages: (a) pyrolysis of avocado biomass under N_2 atmosphere, (b) impregnation of the avocado-based char using an aqueous lithium solution, and (c) thermal activation of lithium-loaded avocado char. Residual avocado biomass was collected from Aguascalientes, Mexico, and used to prepare the adsorbent samples. This precursor was cleaned with hot deionized water to remove residues and soluble impurities and dried for 48 h at 50 °C until a constant weight was achieved. Biomass particles of 0.4–0.5 mm were pyrolyzed to obtain both char and activated carbon samples. Nine activated carbon samples were prepared by applying the experimental conditions reported in Table 1. Seven parameters were involved in the preparation of activated carbons, which were assessed to identify their impact on H_2 adsorption properties and to select their best values. Specifically, the temperature (600–900 h) and dwell time (1–3 h) of the avocado biomass pyrolysis were analyzed to obtain the chars. The concentration (10–50 mg/L) of lithium carbonate solution (HPS, North Charleston, SC, USA), the mass ratio (1/10–1/30 g/mL) of char with respect to volume of lithium solution, and the contact time (3–8 h) utilized to impregnate the avocado char surface were also assessed. The temperature (400–800 °C) and time (1–3 h) of the thermal activation to obtain the activated carbons complete the set of tested synthesis parameters. All experiments listed in Table 1 for preparing the activated carbon samples were performed as follows. First, the avocado biomass particles were pyrolyzed in a tubular furnace (Carbolite, Derbyshire, UK) at a heating rate of 10 °C/min under a N_2 flow of 400 mL/min. Lithium impregnation of avocado chars was carried out at 30 °C using an automatic rotary evaporator (IKA, Staufen, Germany) under constant stirring at 130 rpm. The lithium-impregnated samples were washed with deionized water to remove any excess chemicals and dried for 24 h at 100 °C. Thermal activation of the lithium-loaded chars was carried out under a N_2 atmosphere (400 mL/min) using the tubular furnace at a heating rate of 10 °C/min. All chars and activated carbons were washed with deionized water until a constant pH was obtained in the wastewater and dried for 24 h at 100 °C.

Table 1. Pyrolysis and activation conditions to prepare activated carbons (samples A), from avocado biomass, for H_2 adsorption.

	Pyrolysis		Impregnation with Lithium Solution			Thermal Activation	
Sample	**Temperature, °C**	**Time, h**	**[Li], mg/L**	**Char/Solution Ratio, g/mL**	**Time, h**	**Temperature, °C**	**Time, h**
A1	600	1	10	1/10	3	400	1
A2	600	1	25	1/10	5	800	3
A3	600	2	50	1/20	8	600	3
A4	750	2	10	1/30	8	400	2
A5	750	3	25	1/30	3	800	2
A6	750	3	50	1/10	3	600	1
A7	900	1	10	1/20	5	400	1
A8	900	2	25	1/20	5	600	2
A9	900	3	50	1/30	8	800	3

H_2 adsorption was measured using an Autosorb iQ2-C Series/Quantachrome equipment (Anton Paar, Ashland, VA, USA) and 0.1 g of the tested materials. Degassing of chars and activated carbons was performed for 24 h at 120 °C under vacuum and once the degassing cycle was complete, the samples were gradually cooled to room temperature. H_2 adsorption isotherms were quantified at 77 K and a relative pressure range of 0.1–0.8 atm, reporting the adsorption capacities (q_{H2}) in cm^3/g. H_2 adsorption results were used in the signal-to-noise (S/N) analysis of the experimental design shown in Table 1. This analysis

was applied to establish the impact of activation conditions and to define the best route for enhancing the performance of activated carbon for the storage of H_2 via the maximization of S/N values.

$$S/N = 10\ log\left[\frac{1}{q_{H_2}^2}\right] \quad (1)$$

S/N analysis was also performed using the results from char samples to determine the role of pyrolysis conditions in developing H_2 storage properties. The selected char and activated carbon samples were characterized using X-ray diffraction (XRD), Fourier-transform infrared spectroscopy (FTIR), scanning electron microscopy (SEM), N_2 physisorption, elemental analysis, and X-ray photoelectron spectroscopy (XPS). Details of these characterization techniques, including the conditions for analyzing the samples, are reported in the Supporting Information.

2.2. H_2 Adsorption Mechanism Analysis

Density functional theory (DFT) simulations were performed to characterize the atomic interactions involved in H_2 adsorption on the surface of activated carbon, including the saturation of its active sites via multilayer formation. A finite graphene (G) sheet model functionalized with COOH (G_{COOH}), CO (G_{CO}), and OH (G_{OH}) groups was applied to simulate the activated carbon base structure [32]. Oxidized and Li-decorated graphene structures were considered in these simulations. Full geometrical optimization of all systems was carried out using the Kohn-Sham scheme at the PBE-D3/Def2-SVP level of theory [33–36], with counterpoise corrections applied to account for the basis set superposition error (BSSE) [37]. The adsorption energies of the molecular complexes were calculated to analyze the interactions between G systems and H_2 molecules. This analysis also enables the determination of the energetic stability of H_2 adsorption and the saturation point as the number of adsorbed H_2 molecules increases. The supermolecule approximation $E_{ads} = E_{Gx\text{-}H2} - (E_{H2} + E_{Gx})$ was used for this purpose. The saturated case was analyzed using $E_{ads} = (E_{Gx\text{-}H2} - (nE_{H2} + E_{Gx}))/n$, where $E(_{Gx\text{-}H2})$ corresponds to the energy of the system $(G_x) - H_2$ (x = CO, OH, COOH), while E_{Gx} and E_{H2} are the energies of G_x (x = CO, OH, COOH) and H_2 molecules, respectively. Here, n corresponds to the number of H_2 molecules adsorbed, which ranged from 1 to 5 in the simulations reported in this study. Finally, an Independent Gradient Model (IGM) analysis [38] was applied to gain insights into the nature of interactions. The electronic and scalar field calculations were carried out using ORCA (version 5.0) and Multiwfn (version 3.8) programs [39–41], while the molecular structures were visualized utilizing VMD (version 1.9) software [42]. The results from DFT simulations were used to select an appropriate statistical physics model [43] for calculating the physicochemical parameters related to H_2 adsorption mechanism.

3. Results

3.1. Hydrogen Adsorption Using Chars and Activated Carbons Prepared from Avocado Biomass

Figure 1 shows the experimental isotherms for H_2 adsorption using chars (samples C) at 77 K. Overall, the maximum H_2 adsorption capacities of these samples ranged from 70 to 77 cm^3/g. The char that showed the best H_2 adsorption was obtained at 900 °C for 3 h, while the adsorbent prepared from avocado pyrolysis at 600 °C for 1 h displayed the worst storage capacity. S/N analysis of char preparation conditions is shown in Figure 2.

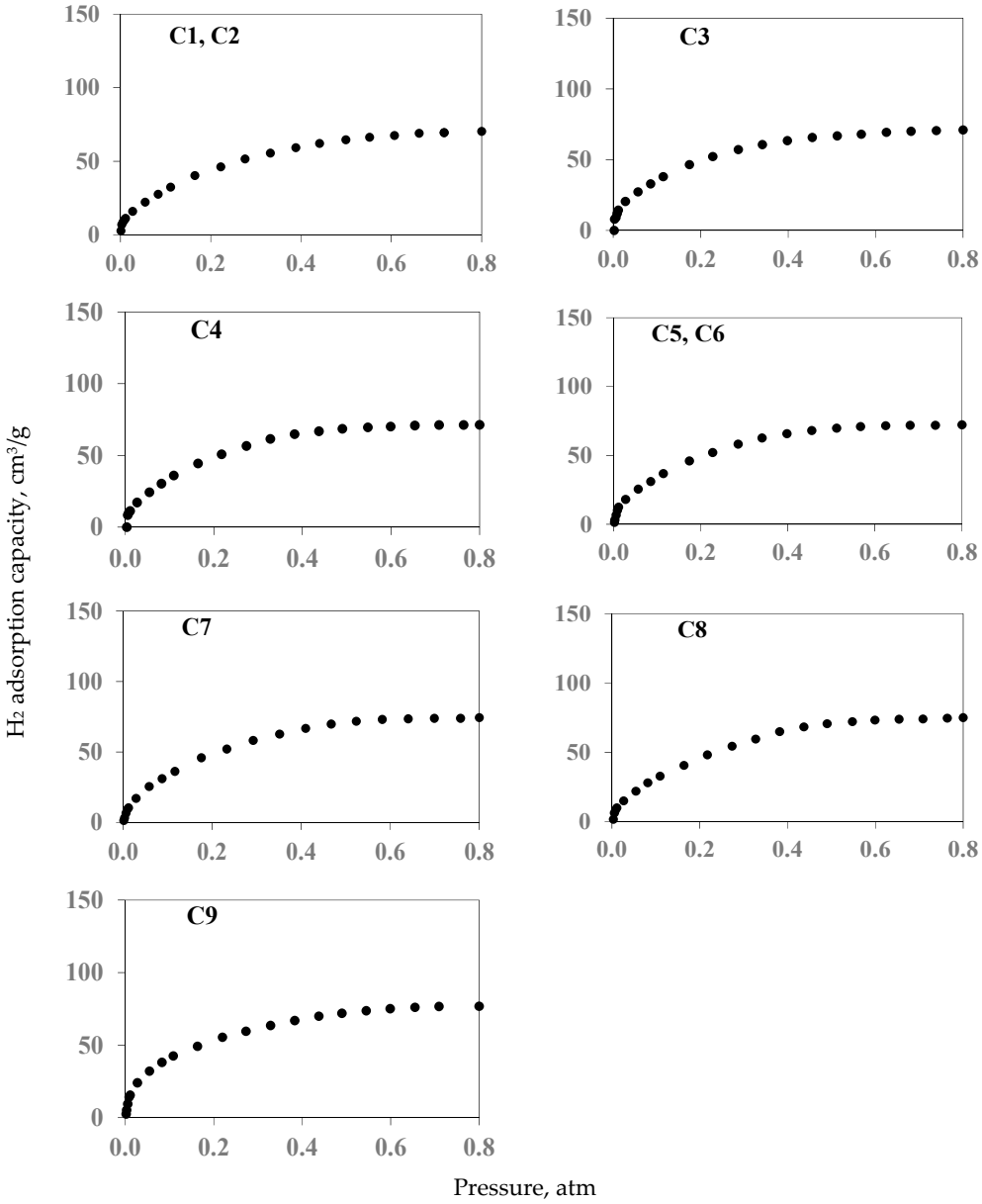

Figure 1. H_2 adsorption isotherms at 77 K using chars (samples C) obtained from avocado residues. (●) Experimental data.

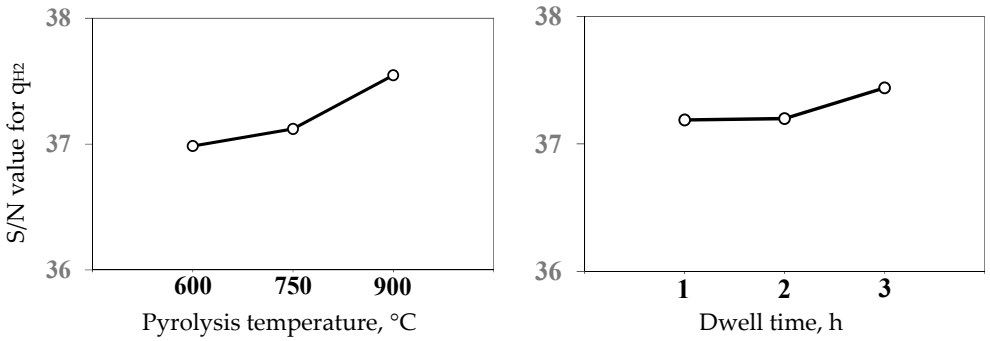

Figure 2. S/N analysis for H_2 adsorption capacity of chars (samples C) obtained from avocado residues.

It was observed that H_2 adsorption increased by 10% for adsorbents obtained at higher pyrolysis temperatures because the development of better textural parameters was favored under more drastic preparation conditions [44,45]. The same trend was observed

for dwell time utilized in avocado waste pyrolysis, although its impact was less significant on H_2 adsorption capacity of the tested chars. The yields of avocado biomass pyrolysis for preparing samples C ranged from 22 to 28%, with the highest values obtained at lower temperatures and dwell times. Overall, the char yield decreased as the biomass pyrolysis temperature increased. This trend also prevailed over the dwell time, where a longer duration of biomass thermal treatment generated lower char yields. The thermal degradation and volatilization of natural polymers (i.e., cellulose, lignin, and hemicellulose) from avocado biomass generated this behavior [46]. These results are consistent with those of previous studies on lignocellulosic biomass pyrolysis [47,48]. For example, Sanchez et al. [47] studied the pyrolysis of biomass residues and obtained char yields of 20–25% at 700–900 °C, while Hoinacki et al. [48] reported yields of 23–26% for preparing carbonaceous materials via the pyrolysis of avocado waste.

The maximum adsorption capacities of activated carbons (samples A) ranged from 121 to 142 cm^3/g, as shown in Figure 3. These results demonstrate that samples A displayed adsorption capacities higher than their counterparts (i.e., samples C) by 71–91% owing to the applied activation conditions. Sample A9 exhibited the highest H_2 storage capacity. This material was prepared via avocado pyrolysis at 900 °C for 3 h, followed by char impregnation with 50 mg/L lithium solution, char/solution ratio of 1/30 g/mL and 8 h of contact time, and thermal activation at 800 °C for 3 h. This activated carbon sample can compete in H_2 storage because its adsorption capabilities are comparable to or even better than those reported in the literature for other carbonaceous adsorbents from residual biomass [49,50]. Previous studies have reported that H_2 adsorption properties of activated carbons prepared from biomass waste usually range from 70 to 140 cm^3/g at 77 K, depending on the feedstock and synthesis route of the adsorbents. In contrast, sample A1 was obtained under the mildest conditions from Table 1, and it exhibited the lowest H_2 adsorption capacity (i.e., 121 cm^3/g) of the nine activated carbon samples tested in this study. The adsorption capacities of the worst (A1) and best (A9) samples of activated carbons differed by 18%.

Figure 4 shows the S/N analysis of the activated carbon synthesis. A clear relationship between the H_2 adsorption capacity of samples A and the avocado biomass pyrolysis temperature, concentration of lithium solution applied for char treatment, and activation temperature was observed. This set of variables played a more important role in the development of H_2 storage properties of activated carbons because of their contribution to generating functional groups (oxygenated and potentially lithium-based functionalities) on both the external and internal surfaces of the adsorbent that act as active sites for H_2 binding. The activation temperature is expected to promote the formation of active sites with a higher affinity for H_2 [51]. The remaining variables assessed in activated carbon synthesis had a limited impact on H_2 adsorption properties. However, a general trend was observed in which the extreme synthesis conditions listed in Table 1 favored H_2 adsorption. Several authors have indicated that the surface activation of chars and other carbonaceous materials is crucial for improving their storage performance [52,53]. For instance, Schaefer et al. [53] modified the surface properties of char obtained from olive stones using KOH to increase H_2 adsorption.

The surface chemistry characterization of selected C and A samples is shown in Figures 5 and 6. XRD patterns shown in Figure 5 correspond to char samples C1, C7 and C9 and activated carbon samples A1, A7 and A9. All adsorbents exhibited two characteristic diffraction peaks of poorly ordered graphitic carbon at ~23° (002) and ~43° (100) 2θ [54]. However, samples A showed an increase in material crystallinity, which was correlated with the activation conditions. In general, the application of high activation temperature and time promotes better structural ordering within the graphitic structure [54,55]. The crystallinity of

activated carbon samples also increased as the concentration of the lithium solution used to modify the adsorbent surface increased, although no diffraction peaks associated with crystalline Li-containing phases were identified. This behavior may suggest that lithium is highly dispersed within the carbon matrix [56]. These results are consistent with those reported by Lui et al. [56], Cho et al. [57] and Ma et al. [58] for Li-functionalized materials.

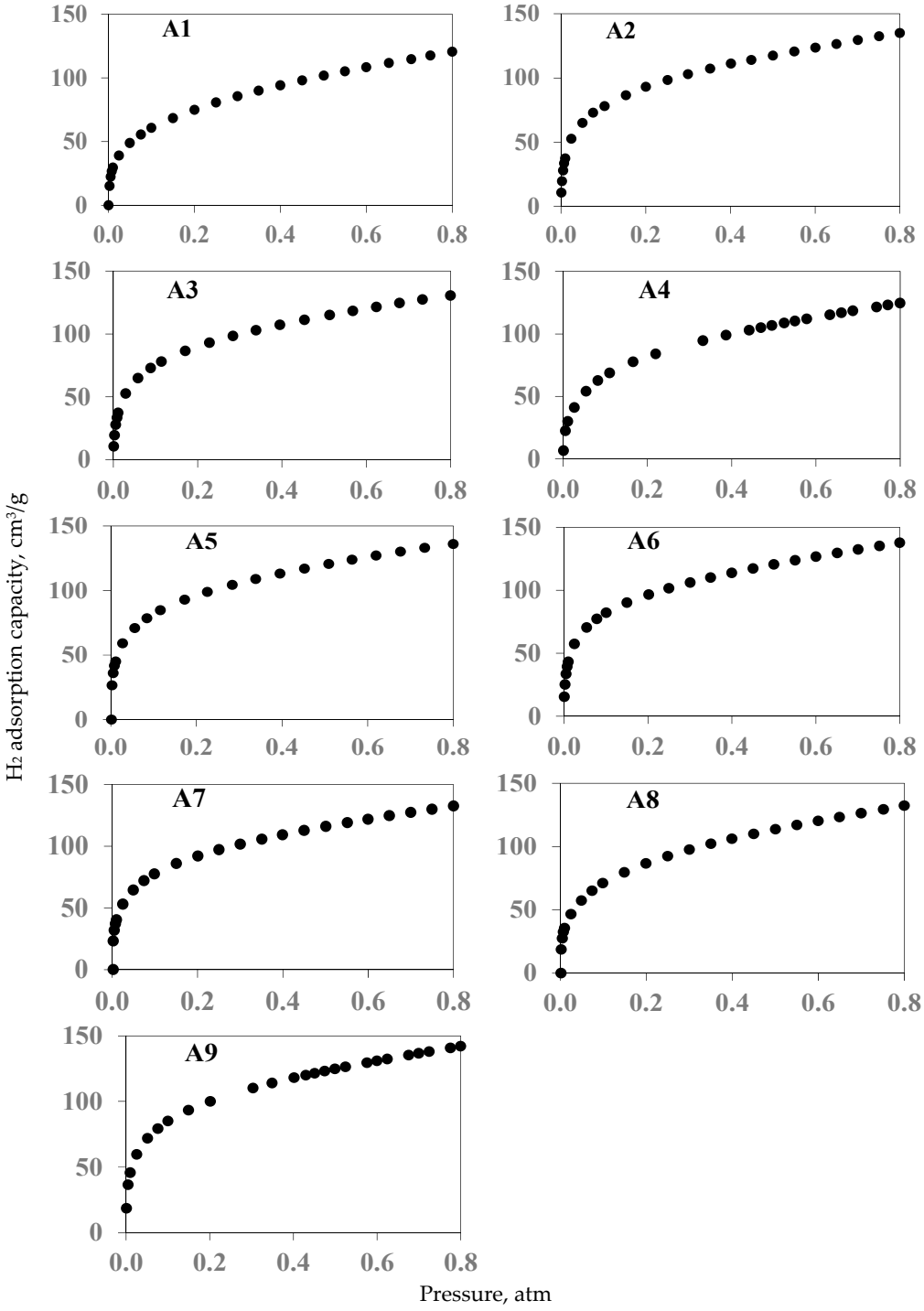

Figure 3. H_2 adsorption isotherms at 77 K using activated carbons (samples A) obtained from avocado residues. (•) Experimental data.

FTIR spectra of samples C and A are reported in Figure 5. All materials exhibited an absorption band at ~3450 cm^{-1} attributed to O-H stretching vibrations of phenols and alcohols [59]. The absorption bands at ~2940–2870 and ~1435 cm^{-1} are associated with C-H

and C=C stretching vibrations, respectively, of aliphatic structures [58]. C=O stretching vibrations of carboxylic acids and/or C=C stretching vibrations in aromatic structures are identified at ~1625 cm^{-1} [59,60]. The absorption band of C=C stretching vibration of aromatic compounds is observed at ~1530 cm^{-1} [61], while the bands located at ~1371, 1210, 1080, 955, 871–755 and 655 cm^{-1} are related to O-H (bending), C-O (stretching) and C-H (bending) vibrations of phenols, alcohols, ethers, esters and aromatic structures in carbon-based materials [60–62]. The intensity of some absorption bands changed after activation, suggesting slight variations in the concentration or chemical environment of the surface functional groups. Lithium may be deposited on the oxygen-containing functional groups of the carbon surface without the formation of dendrites [63], where carboxyl-based moieties play a dominant role in governing interactions with lithium [64–66].

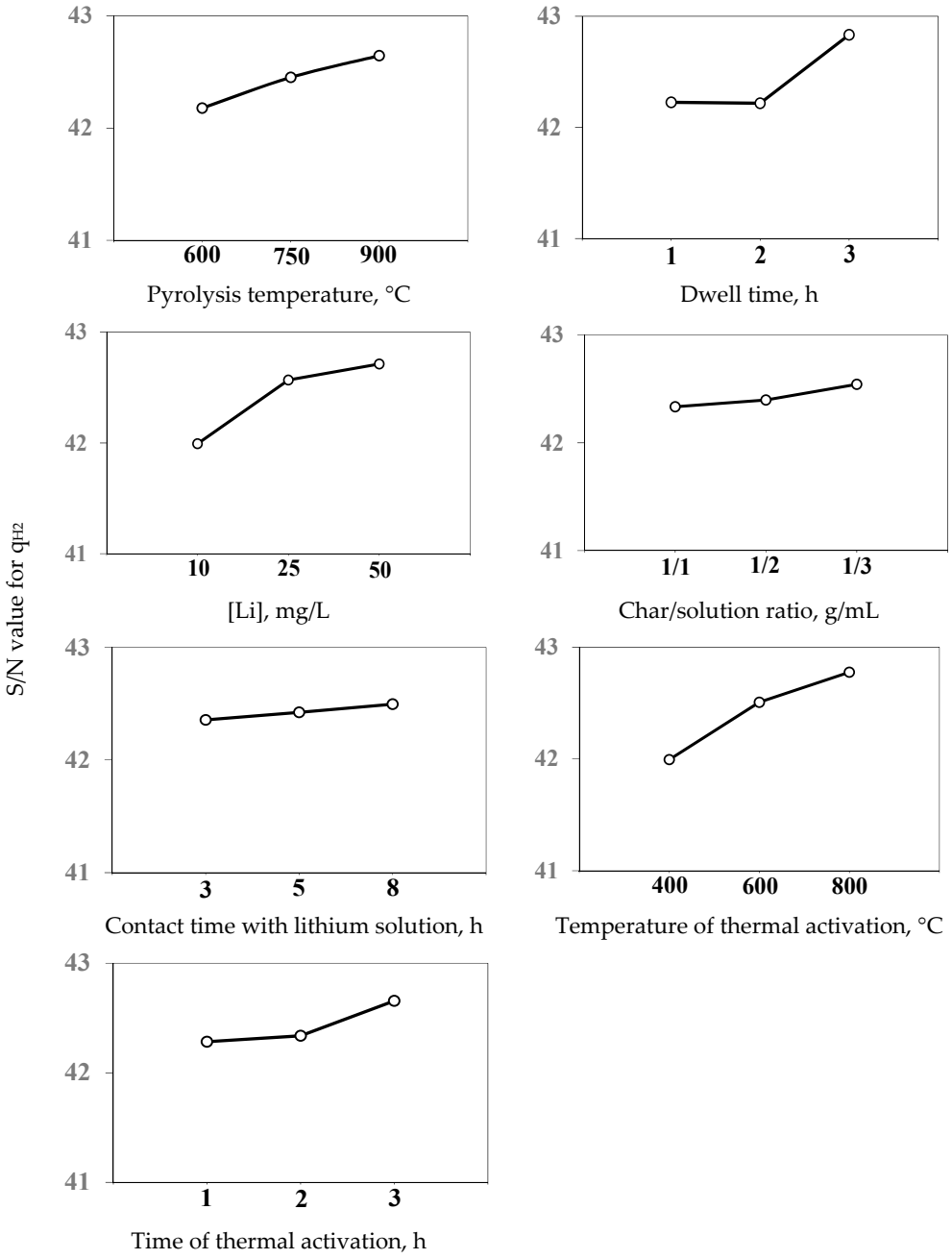

Figure 4. S/N analysis for H_2 adsorption capacity of activated carbons (samples A) obtained from avocado residues.

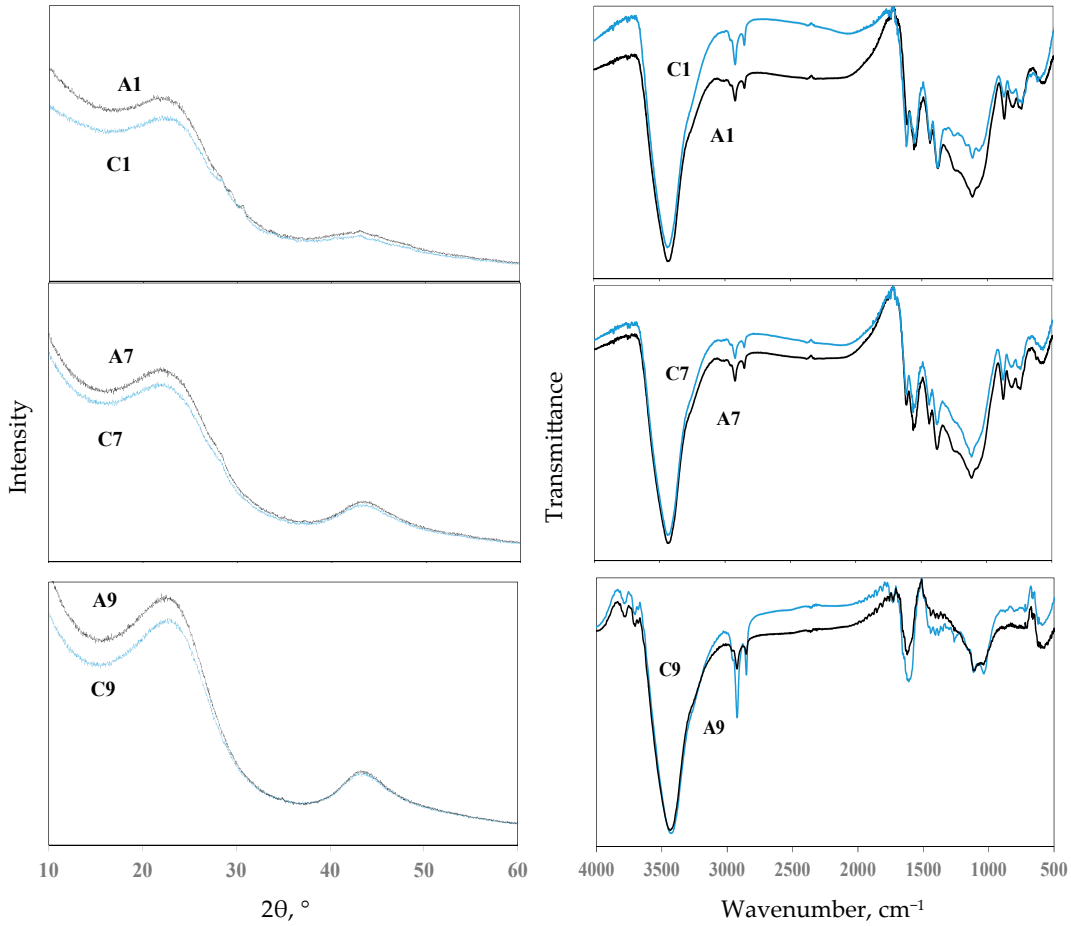

Figure 5. XRD and FTIR results of chars (samples C) and activated carbons (samples A) used in H_2 adsorption.

XPS analysis revealed no significant variations in either bond energies or the relative peak intensities when comparing the chars with activated carbons. The high-resolution C1s spectra of samples C9 and A9 are reported in Figure 6. These spectra were deconvoluted into three peaks corresponding to C=C (284.8 eV), C-O (285.6 eV), and O-C=O (288.7 eV) bonds [66]. In contrast, the high-resolution O 1s spectra contained a single peak attributed to C-O/C=O (532.7 eV) bonds [67,68] for both adsorbent samples. These results suggest that activation may affect the local coordination or protonation state of existing oxygen-containing moieties (as suggested by infrared spectra) but does not induce significant alterations in the overall chemical environment of carbon- and oxygen-containing surface species.

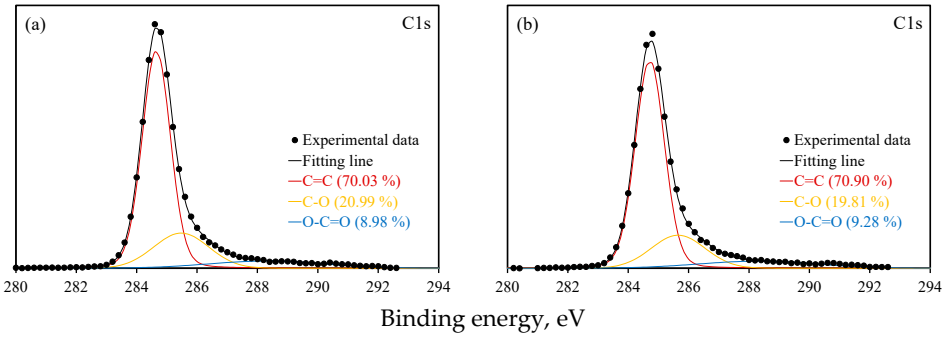

Figure 6. High–resolution C1s XPS spectra of (**a**) char C9 and (**b**) activated carbon A9 used in H_2 adsorption.

SEM images illustrating the morphologies of the char and activated carbon samples are shown in Figure 7, while the elemental compositions of the selected char and activated carbon samples are reported in Table 2. It was found that a higher pyrolysis temperature resulted in a more graphitized material with higher C and N contents and lower H and O contents. The activation process apparently led to oxidation or an increase in the mineral matter in the samples activated at higher temperatures. SEM/EDX results also confirmed the high graphitization (C content > 80%) of the adsorbents, while other trace elements were identified. The textural parameters of the activated carbon samples are listed in Table 3. BET surface areas of these adsorbents ranged from 50 to 173 m^2/g, with micropore and mesopore volumes of 0.017–0.058 and 0.078–0.125 cm^3/g, respectively. The activation conditions increased both the mesopores and micropores. In contrast, the chars showed low porosity, which partially explains their lower H_2 adsorption capacities.

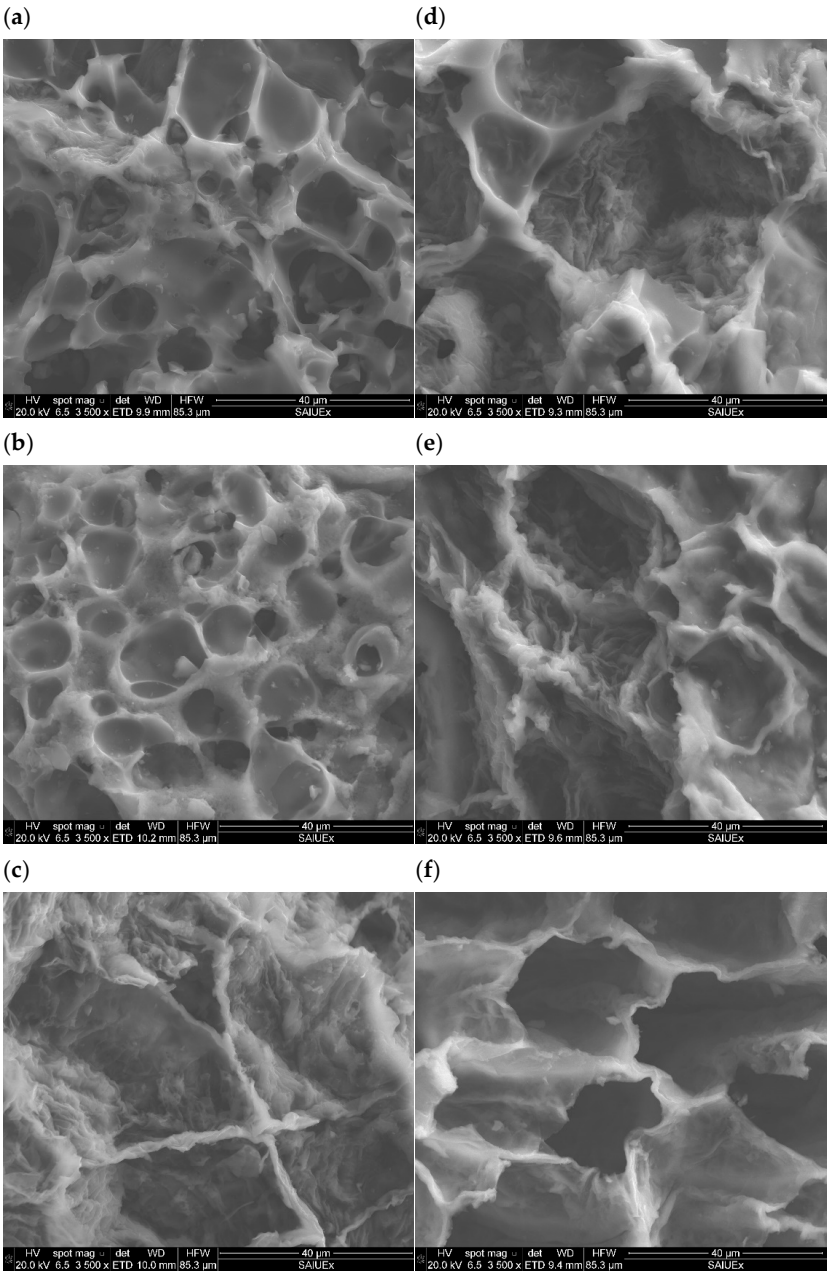

Figure 7. SEM images (3500× magnification) of selected samples of chars (samples C) and activated carbons (samples A) used in H_2 adsorption. (**a**) C1; (**b**) C3; (**c**) C8; (**d**) A1; (**e**) A3; (**f**) A9.

Table 2. Elemental composition of chars (samples C) and activated carbons (samples A) used in H_2 adsorption.

CHNO Analysis, %					SEM/EDX Analysis, %									
Sample	**C**	**H**	**N**	**O_{diff}**	**C**	**O**	**Na**	**Mg**	**Al**	**P**	**S**	**K**	**Ca**	**Cl**
C1	82.16	3.93	1.23	12.68	88.60	8.32	-	0.26	-	0.49	0.12	2.14	0.35	-
C3	80.01	4.17	1.21	14.61	86.61	10.70	-	0.29	-	0.52	0.13	1.69	0.27	-
C8	85.11	2.68	1.76	10.45	93.58	5.43	-	0.23	0.25	0.23	-	0.18	0.25	-
A1	85.61	4.34	1.66	8.39	88.38	10.12	-	0.27	0.06	0.23	-	-	-	0.49
A3	83.31	3.27	1.69	11.73	88.48	10.74	0.10	0.22	0.47	0.14	-	-	-	0.07
A9	83.19	2.48	1.63	12.70	88.30	7.64	0.09	0.14	-	2.87	0.07	-	-	-

The results highlight the relevance of both textural parameters and surface chemistry to enhance H_2 adsorption properties of carbonaceous adsorbents. Herein, it is convenient to remark that KOH is an effective chemical for developing the textural properties of activated carbons; however, its main limitations are its aggressive and corrosive properties, which require special materials for the reactors to perform the activation process [69]. This activation route is usually performed at high temperatures (>900 °C) to be effective and produces a significant quantity of inorganic residues on the final adsorbent that must be removed via washing with water and acid solutions, thus generating wastewater with high pH and salinity [70]. Therefore, the carbon footprint of the KOH activation route is expected to be significantly higher than that of other adsorbent preparation methods, and its operational costs may be unjustifiable for industrial applications. In contrast, the proposed activation route uses milder operating conditions and avoids the use of corrosive chemicals, which may generate technoeconomic benefits. However, a life cycle assessment is required to determine and compare the limitations and advantages of this activation protocol and others. The surface functionalization of activated carbons is also a key parameter for obtaining effective H_2 adsorbents. The incorporation of other heteroatoms (e.g., N, S, and P) and multivalent metals into the activated carbon structure can also help to improve H_2 storage [22], thus opening the possibility of developing a wide spectrum of adsorbent preparation protocols. Further studies are required to test other activation routes, incorporate different active sites on the activated carbon surface, analyze and understand their roles in the H_2 adsorption mechanism.

Table 3. Textural parameters of activated carbons (samples A) used in H_2 adsorption.

		Pore Volume, cm^3/g		
Sample	**BET Area, m^2/g**	**Micropore**	**Mesopore**	**Total**
A1	50	0.017	0.043	0.078
A3	88	0.020	0.125	0.144
A9	173	0.058	0.110	0.192

3.2. H_2 Adsorption Mechanism Modeling

This section focuses on the discussion of the results of the modeling of H_2 adsorption from an electronic structure perspective. In general, DFT simulations indicated that when the H_2 molecule approaches the carbonaceous sheet, it is not positioned on the surface; instead, it preferentially localizes in the vicinity of oxygen-containing functional groups, where the electronic density is more heterogeneous, generating weak intermolecular binding; see Figure 8. For the $G_{CO\text{-}H2}$ complex, an interaction length of 2.54 Å and a nearly linear orientation, with an angle of 175°, are observed. These values agree with those of previous theoretical studies [71]. $G_{OH\text{-}H2}$ and $G_{COOH\text{-}H2}$ systems exhibited a slight reduction in

interaction distance and angular linearity with values of 2.65 Å and 168° for G_{OH-H2}, and 2.67 Å and 158° for $G_{COOH-H2}$, respectively. These differences are due to the presence of oxygenated groups that alter the electronic distribution in the graphene sheet, generating a major charge density in adjacent atoms, which thermodynamically stabilizes the system. Thus, the changes in the linearity of H_2 adsorption modify the local environment and generate polarization effects induced by the oxygenated functional groups, while the interactions remain mainly weak and noncovalent [72].

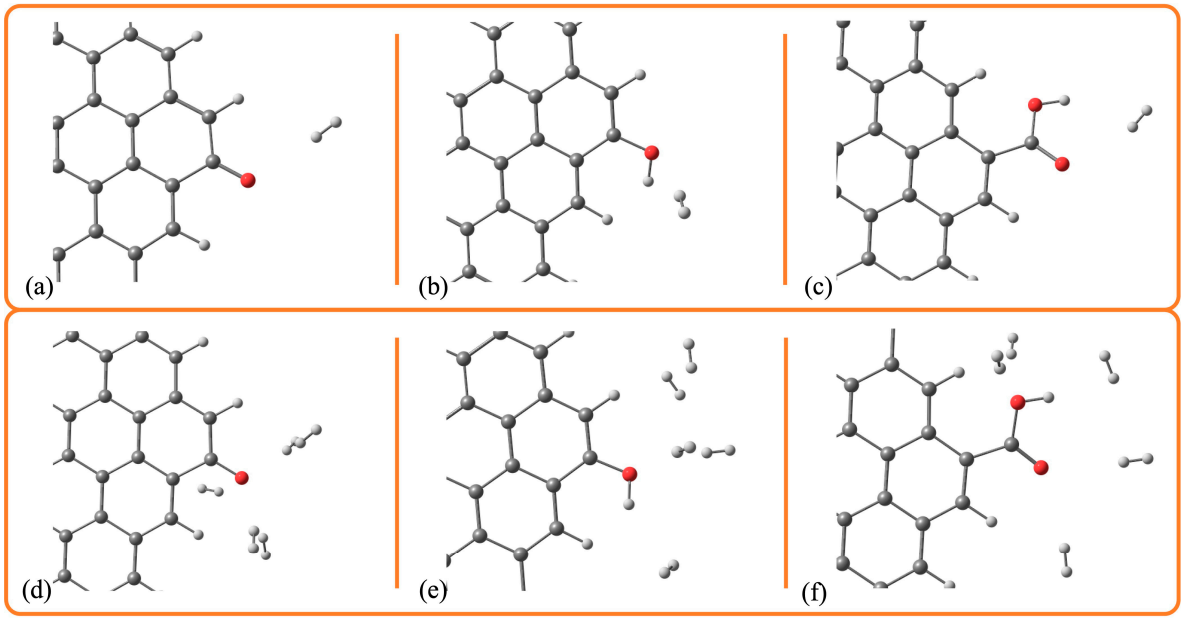

Figure 8. Optimized molecular structures for (**a**) G_{CO-H2}, (**b**) G_{OH-H2}, (**c**) $G_{COOH-H2}$, (**d**) G_{CO-5H2}, (**e**) G_{OH-5H2}, and (**f**) $G_{COOH-5H2}$. Atoms by color: carbon, silver; oxygen, red; hydrogen, white.

The calculated adsorption energies were −0.062, −0.068 and −0.085 eV for G_{OH-H2}, $G_{COOH-H2}$, and G_{CO-H2}, respectively, which are consistent with the structural trends discussed above. These results indicate that H_2 adsorption is governed by weak interactions in all cases, which is characteristic of physisorption, as demonstrated by the IGM analysis (see Figure 9). This behavior can be attributed to the high electronic density of the oxygen atom in the -CO group, whose unshared electron pairs interact with the electronic cloud of H_2, including polarization and improving the intermolecular interaction that contributes significantly to the stability of the graphene-oxygen system [73]. On the other hand, -OH and -COOH groups exhibited adsorption energies associated with weaker interactions. For G_{COOH}, the electronic delocalization between both O atoms decreases the electronic availability of the active site, whereas the strong polarity of -OH affects the interaction with H_2 [73,74]. Note that this behavior changes when multiple H_2 molecules are adsorbed simultaneously, as depicted in Figure 9. Upon saturation with five H_2 molecules, the adsorption energy per molecule decreased by up to 0.035 eV in all systems, indicating that H_2 molecules had less stability in the interaction. This energy reduction can be attributed to the competitive adsorption effects and the steric repulsion between H_2 molecules. Under these conditions, the $G_{COOH-H2}$ system exhibited the most stabilizing interaction, with an adsorption energy of −0.054 eV per H_2, followed by G_{OH-H2} with −0.053 eV, and G_{CO-H2} at −0.050 eV. Despite this decrease, the energies remained within the physisorption range, confirming that the adsorption process is governed by weak, noncovalent interactions. The saturation increases the interaction distances, resulting in adsorption lengths ranging from 2.18 to 3.27 Å. This geometric expansion supports the conclusion that steric effects play a dominant role in saturation, suggesting a possible interaction through multilayer formation.

IGM analysis also indicated that all systems were dominated by weak noncovalent interactions between oxygenated functional groups and H_2 molecules. A simple way to represent noncovalent interactions is by the generation of colored isosurfaces: blue, strong interactions (hydrogen bonds, electrostatic), green, weak interactions (dispersive, van der Waals), red, repulsive interactions (steric, among others) [38]. Therefore, this adsorption mechanism can be explained by the attraction between -CO, -OH, and -COOH functionalities and H_2 molecules, where the high electronegativity of the oxygen atoms induces a transitory polarization in the graphene, generating dispersive interactions and an induced dipole type [71,75].

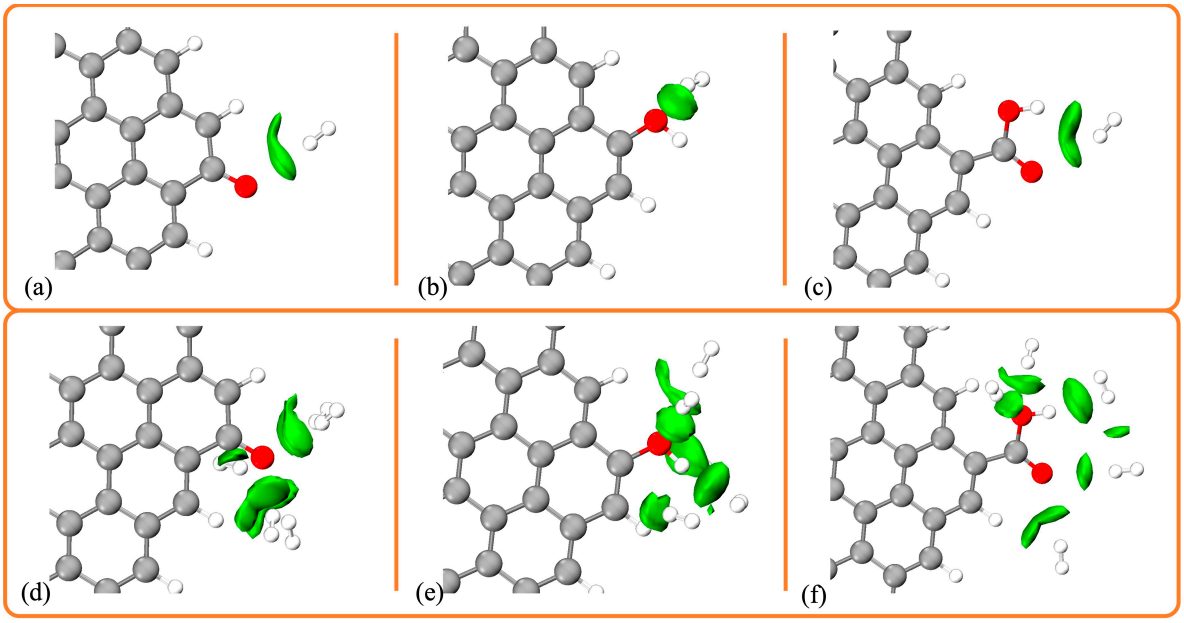

Figure 9. Independent Gradient Model (IGM) analysis for (**a**) $G_{CO\text{-}H2}$, (**b**) $G_{OH\text{-}H2}$, (**c**) $G_{COOH\text{-}H2}$, (**d**) $G_{CO\text{-}5H2}$, (**e**) $G_{OH\text{-}5H2}$, and (**f**) $G_{COOH\text{-}5H2}$. Atoms by color: carbon, silver; oxygen, red; hydrogen, white.

DFT simulations also showed that the incorporation of alkaline metals, such as Li may increase the adsorption energy from −0.2 to −0.4 eV, due to the polarization induced by the metallic cation on H_2 molecules, which favors weak electric polarization interactions and promotes their attraction [76,77]. Figure 10 shows that Li cation binds to the oxygenated functional groups mainly through electrostatic interactions. This interaction induces a bond elongation of the functional groups: C=O bond length increases from 1.25 to 1.88 Å, O-H bond from 1.33 to 1.92 Å, and carboxyl C=O bond from 1.22 to 1.66 Å. This elongation can be attributable to the partial transfer of electronic density from O to Li, decreasing the possible covalent character of the bond as reported by Srinivasu and Ghosh [78]. The calculated adsorption energies revealed a significant stabilization of the system upon Li incorporation, with values of −0.17 eV for $G_{CO\text{-}Li\text{-}H2}$, −0.18 eV for $G_{COOH\text{-}Li\text{-}H2}$, and −0.19 eV for $G_{OH\text{-}Li\text{-}H2}$. These energy values are associated with the local redistribution of electronic density, where Li acts as a site with a positive charge capable of polarizing H_2 molecules [79]. IGM analysis of these systems is reported in Figure 11, where isosurfaces associated with electrostatic and van der Waals interactions are observed between all H_2 molecules, Li, and G_X surfaces. Noncovalent interactions between neighboring H_2 molecules were also identified. This result suggests a possible cooperative adsorption effect where H_2-H_2 interaction contributes to the overall stabilization of the system through the formation of multiple-shell interactions [80,81]. Therefore, cooperative effects can enhance the H_2 adsorption capacity of $G_{X\text{-}Li}$ systems.

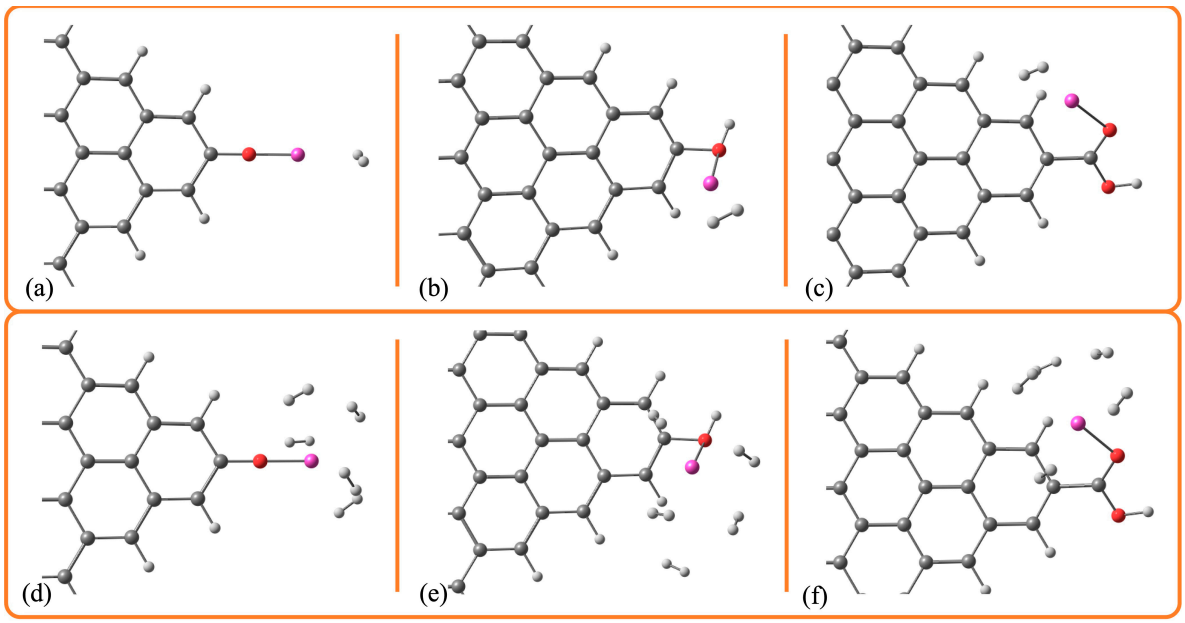

Figure 10. Optimized structures for (**a**) $G_{CO\text{-}Li\text{-}H2}$, (**b**) $G_{OH\text{-}Li\text{-}H2}$, (**c**) $G_{COOH\text{-}H2}$, (**d**) $G_{CO\text{-}Li\text{-}5H2}$, (**e**) $G_{OH\text{-}Li\text{-}5H2}$, and (**f**) $G_{COOH\text{-}Li\text{-}5H2}$. Atoms by color: carbon, silver; oxygen, red; lithium, pink; hydrogen, white.

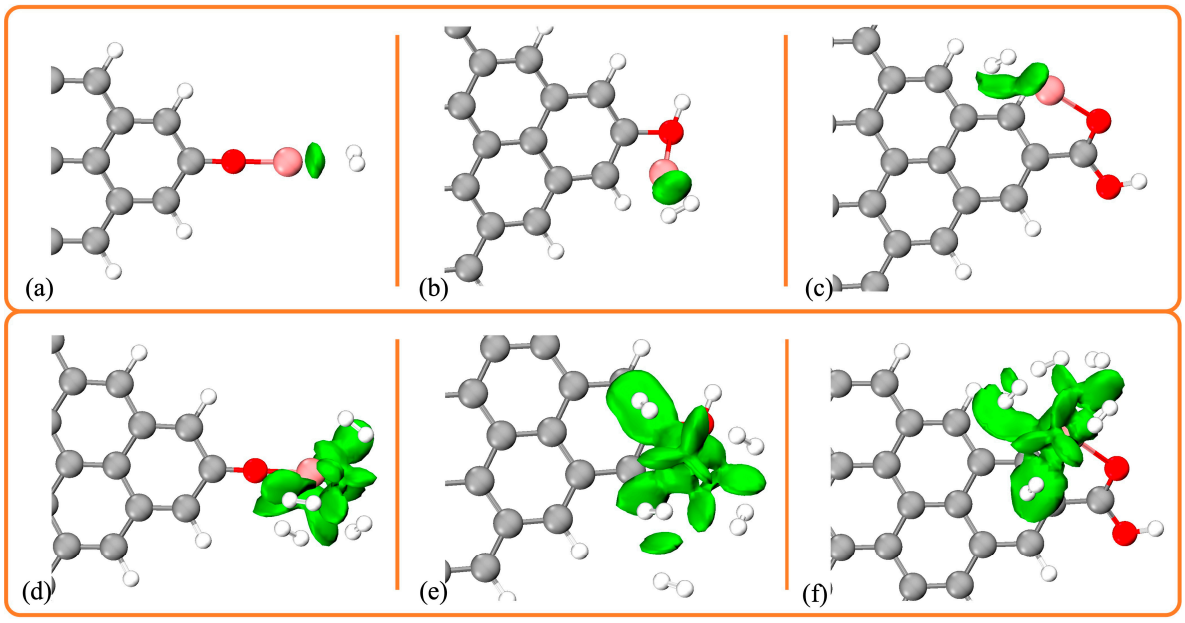

Figure 11. Independent Gradient Model (IGM) analysis for (**a**) $G_{CO\text{-}Li\text{-}H2}$, (**b**) $G_{OH\text{-}Li\text{-}H2}$, (**c**) $G_{COOH\text{-}Li\text{-}H2}$, (**d**) $G_{CO\text{-}Li\text{-}5H2}$, (**e**) $G_{OH\text{-}Li\text{-}5H2}$, and (**f**) $G_{COOH\text{-}Li\text{-}5H2}$. Atoms by color: carbon, silver; oxygen, red; lithium, pink; hydrogen, white.

A multilayer statistical physics model was applied to estimate the number (N_{LH2}) of adsorbed H_2 layers formed on the activated carbon surface, the number (n_{H2}) of H_2 molecules adsorbed per active site, and the concentration of active sites (AS_{H2}, mmol/g) of activated carbon participating in H_2 storage. This multilayer model is given by

$$q_{H_2} = n_{H_2} \cdot AS_{H_2} \cdot \theta_1 \quad (2)$$

where θ_1 is defined in Supporting Information. The correlation of H_2 isotherms was performed using q_{H2} in mmol/g, and the results are reported in Table 4. The isotherm

modeling results confirmed that H_2 storage on samples A implied a multilayer adsorption forming from 2 to 4 layers on the surfaces of the tested activated carbons. Molecular aggregation of H_2 can also occur with the potential formation of dimers and trimers during adsorption. The calculated values of AS_{H2} were 0.83–1.21 mmol/g, as shown in Table 4.

Table 4. Calculated physicochemical parameters for the multilayer adsorption of H_2 on activated carbons (samples A) used in this study.

Sample	n_{H2}	AS_{H2}, mmol/g	N_{LH2}
A1	1.98	0.96	2.9
A2	2.21	0.83	3.2
A3	2.15	0.87	3.2
A4	2.17	0.67	3.5
A5	2.10	1.21	2.4
A6	2.36	0.84	3.0
A7	2.10	1.10	2.5
A8	2.05	1.04	2.7
A9	2.53	0.85	2.8

4. Conclusions

The preparation conditions of chars and activated carbons from avocado residues were tailored to maximize their hydrogen adsorption properties. An activation protocol based on lithium functionalization and thermal treatment improves the adsorption capacities of carbon-based adsorbents obtained from avocado waste for hydrogen storage. The characterization and modelling results showed that physisorption may play a relevant role in the multilayer adsorption of hydrogen on the tested materials. Oxygenated active sites on activated carbon surface can adsorb 2 or 3 hydrogen molecules. In particular, the presence of physical interactions in the hydrogen adsorption mechanism is beneficial for the application of avocado-based adsorbents in green hydrogen storage systems because desorption can be performed via depressurization. This study contributes experimental and modelling results to promote the application of low-cost activated carbons in the green hydrogen supply chain.

Supplementary Materials: The following supporting information can be downloaded at https://www.mdpi.com/article/10.3390/c12010005/s1, which included details of characterization techniques and equipment and the statistical physics model description.

Author Contributions: Conceptualization, Z.V.H.-C., A.B.-P. and L.J.B.-S.; methodology, Z.V.H.-C. and L.J.B.-S.; formal analysis, Z.V.H.-C., A.B.-P., C.J.D.-V. and L.J.B.-S.; investigation, Z.V.H.-C., L.J.B.-S., E.G.-H., C.J.D.-V. and A.B.-P.; resources, A.B.-P.; writing—original draft preparation, A.B.-P., D.I.M.-C., C.J.D.-V. and E.G.-H.; writing—review and editing, A.B.-P., D.I.M.-C., C.J.D.-V., H.E.R.-Á., M.d.R.M.-V., G.S.-F., S.A.-R. and E.G.-H.; project administration, A.B.-P. All authors have read and agreed to the published version of the manuscript.

Funding: This research was funded by Tecnológico Nacional de México (grant number 21505.25-P), European Union (European Regional Development Fund), and Junta de Extremadura (grant number GR24050).

Data Availability Statement: The original contributions presented in this study are included in the article/Supplementary Material. Further inquiries can be directed to the corresponding author.

Acknowledgments: Authors acknowledge the support provided by IBERBIOMASA and #MatPore networks.

Conflicts of Interest: The authors declare no conflicts of interest.

References

1. Jensen, L.L.; Bonnefoy, P.A.; Hileman, J.I.; Fitzgerald, J.T. The carbon dioxide challenge facing U.S. aviation and paths to achieve net zero emissions by 2050. *Prog. Aerosp. Sci.* **2023**, *141*, 100921. [CrossRef]
2. Kouchaki-Penchah, H.; Bahn, O.; Bashiri, H.; Bedard, S.; Bernier, E.; Elliot, T.; Hammache, A.; Vaillancourt, K.; Levasseur, A. The role of hydrogen in a net-zero emission economy under alternative policy scenarios. *Int. J. Hydrogen Energy* **2023**, *49*, 173–187. [CrossRef]
3. Ahmad, S.; Ullah, A.; Samreen, A.; Qasim, M.; Nawaz, K.; Ahmad, W.; Alnaser, A.; Kannan, A.M.; Egilmez, M. Hydrogen production, storage, transportation and utilization for energy sector: A current status review. *J. Energy Storage* **2024**, *101*, 113733. [CrossRef]
4. Brahim, T.; Jemni, A. Green hydrogen production: A review of technologies, challenges, and hybrid system optimization. *Renew. Sustain. Energy Rev.* **2026**, *225*, 116194. [CrossRef]
5. Mansilha, C.; Barbosa-Povoa, A.; Tarelho, L.; Fonseca, A. A comprehensive review of green hydrogen production technologies: Current status, challenges, research trends and future. *Renew. Sustain. Energy Rev.* **2026**, *225*, 116119. [CrossRef]
6. Nemmour, A.; Inayat, A.; Janajreh, I.; Ghenai, C. Green hydrogen-based E-fuels (E-methane, E-methanol, E-ammonia) to support clean energy transition: A literature review. *Int. J. Hydrogen Energy* **2023**, *48*, 29011–29033. [CrossRef]
7. Aba, M.M.; Sauer, I.L.; Amado, N.B. Comparative review of hydrogen and electricity as energy carriers for the energy transition. *Int. J. Hydrogen Energy* **2024**, *57*, 660–678. [CrossRef]
8. Muhieitheen, M.K.; Hameed, A.B.S. Exploring hydrogen storage: A review of technologies, challenges, policy incentives, and future directions in renewable integration. *Next Res.* **2025**, *2*, 100658. [CrossRef]
9. Qureshi, F.; Yusuf, M.; Ahmed, S.; Haq, M.; Alraih, A.M.; Hidouri, T.; Kamyab, H.; Vo, D.V.N.; Ibrahim, H. Advancements in sorption-based materials for hydrogen storage and utilization: A comprehensive review. *Energy* **2024**, *309*, 132855. [CrossRef]
10. Sadkhan, R.A.; Al-Mudhafar, W.J. Key aspects of underground hydrogen storage in depleted hydrocarbon reservoirs and saline aquifers: A review and understanding. *Energy Geosci.* **2024**, *5*, 100339. [CrossRef]
11. Sharma, G.; Dewangan, A.K.; Yadav, A.K.; Ahmad, A. Current status of research on hydrogen generation, storage and transportation technologies: A state-of-the-art review towards sustainable energy. *Process Saf. Environ. Prot.* **2024**, *191*, 1445–1460.
12. Ramirez-Vidal, P.; Sdanghi, G.; Celzard, A.; Fierros, V. High hydrogen release by cryo-adsorption and compression on porous materials. *Int. J. Hydrogen Energy* **2022**, *47*, 8892–8915. [CrossRef]
13. Yang, X.; He, H.; Lv, T.; Qiu, J. Fabrication of biomass-based functional carbon materials for energy conversion and storage. *Mater. Sci. Eng. R* **2023**, *154*, 100736. [CrossRef]
14. Li, X.; Ding, Y.; Zhang, H.; He, T.; Hao, J.; Wu, J.; Wu, Y.; Bai, H. Pine sawdust derived ultra-high specific surface area activated carbon: Towards high-performance hydrogen storage and supercapacitors. *Int. J. Hydrogen Energy* **2024**, *84*, 623–633. [CrossRef]
15. Shafeeyan, M.S.; Daud, W.M.A.W.; Houshmand, A.; Shamiri, A. A review on surface modification of activated carbon for carbon dioxide adsorption. *J. Anal. Appl. Pyrolysis* **2010**, *89*, 143–151. [CrossRef]
16. Gopalan, J.; Buthiyappan, A.; Raman, A.A.A. Insight into metal-impregnated biomass based activated carbon for enhanced carbon dioxide adsorption: A review. *J. Ind. Eng. Chem.* **2022**, *113*, 72–95. [CrossRef]
17. De Rose, E.; Bartucci, S.; Bonaventura, C.P.; Conte, G.; Agostino, R.G.; Policicchio, A. Effects of activation temperature and time on porosity features of activated carbons derived from lemon peel and preliminary hydrogen adsorption tests. *Colloids Surf. A Physicochem. Eng. Asp.* **2023**, *672*, 131727. [CrossRef]
18. Elyasi, S.; Saha, S.; Hameed, N.; Mahon, P.J.; Juodkazis, S.; Salim, N. Emerging trends in biomass-derived porous carbon materials for hydrogen storage. *Int. J. Hydrogen Energy* **2024**, *62*, 272–306. [CrossRef]
19. Kong, Z.; Zhang, H.; Zhou, T.; Xie, L.; Wang, B.; Jian, X. Biomass-derived functional materials: Preparation, functionalization and applications in adsorption in catalytic separation of carbon dioxide and other atmospheric pollutants. *Sep. Purif. Technol.* **2025**, *354*, 129099.
20. Yin, Y.; Liu, Q.; Wang, J.; Zhao, Y. Recent insights in synthesis and energy storage applications of porous carbon derived from biomass waste: A review. *Int. J. Hydrogen Energy* **2022**, *47*, 39338–39363. [CrossRef]
21. Lu, S.; Fang, L.; Wang, X.; Liu, T.X.; Zhao, X.; Xu, B.B.; Hua, Q.; Liu, H. Insights into activators on biomass-derived carbon-based composites for electrochemical energy storage. *Mater. Today Chem.* **2024**, *37*, 101988. [CrossRef]
22. Gillani, Q.F.; Bakbolat, B.; Tatykayev, B.; Sultanov, F.; Mentbayeva, A. Biomass-derived carbon materials for hydrogen storage: Structure-performance relationships and design strategies. *J. Energy Storage* **2025**, *135*, 118401. [CrossRef]
23. Khan, S.A.; Ali, S.; Sarfraz, S.; Hussain, S.; Mansha, M. Biomass-derived carbon materials for hydrogen storage: Challenges and future perspectives. *Energy Convers. Manag. X* **2026**, *29*, 101425.
24. Konyannik, B.Y.; Lavie, J.D. Valorization techniques for biomass waste in energy generation: A systematic review. *Bioresour. Technol.* **2025**, *435*, 132973. [CrossRef] [PubMed]
25. Behera, U.S.; Singh, R. Hydrogen storage systems using activated carbon. In *Reference Module in Earth Systems and Environmental Sciences*; Elsevier: Amsterdam, The Netherlands, 2025.

26. Elyasi, S.; Hameed, N.; Mahon, P.J.; Juodkazis, S.; Keshavarz, A.; Iglauer, S.; Matamba, T.; Vongsvivut, J.; Salim, N.V. Analysis of pistachio shell-derived activated porous carbon materials for hydrogen adsorption. *Int. J. Hydrogen Energy* **2025**, *119*, 260–270. [CrossRef]
27. Lionetti, V.; Bartucci, S.; Bonaventura, C.P.; Conte, G.; Desiderio, G.; Policicchio, A.; Agostino, R.G. Optimized activation of coffee-ground carbons for hydrogen storage. *Int. J. Hydrogen Energy* **2025**, *136*, 1029–1040. [CrossRef]
28. Serafin, J.; Dziejarski, B.; Solis, C.; de la Piscina, P.R.; Homs, N. Medium-pressure hydrogen storage on activated carbon derived from biomass conversion. *Fuel* **2024**, *363*, 130975. [CrossRef]
29. Samantaray, S.S.; Mangisetti, S.R.; Ramaprabhu, S. Investigation of room temperature hydrogen storage in biomass derived activated carbon. *J. Alloys Compd.* **2019**, *789*, 800–804. [CrossRef]
30. Cetingurbuz, E.; Turkyilmaz, A. Production of activated carbon by lithium activation and determination of hydrogen storage capacity. *Ind. Crops Prod.* **2023**, *203*, 117171. [CrossRef]
31. Lionetti, V.; Bonaventura, C.P.; Conte, G.; De Luca, O.; Policicchio, A.; Caruso, T.; Desiderio, G.; Papagno, M.; Agostino, R.G. Production and physical-chemical characterization of walnut shell-derived activated carbons for hydrogen storage application. *Int. J. Hydrogen Energy* **2024**, *61*, 639–649. [CrossRef]
32. Cam, L.M.; Van Khu, L.; Ha, N.N. Theoretical study on the adsorption of phenol on activated carbon using density functional theory. *J. Mol. Model.* **2013**, *19*, 4395–4402. [CrossRef]
33. Schäfer, A.; Horn, H.; Ahlrichs, R. Fully optimized contracted Gaussian basis sets for atoms Li to Kr. *J. Chem. Phys.* **1992**, *97*, 2571–2577. [CrossRef]
34. Perdew, J.P.; Burke, K.; Ernzerhof, M. Generalized gradient approximation made simple. *Phys. Rev. Lett.* **1996**, *77*, 3865. [CrossRef] [PubMed]
35. Grimme, S.; Antony, J.; Ehrlich, S.; Krieg, H. A consistent and accurate ab initio parametrization of density functional dispersion correction (DFT-D) for the 94 elements H-Pu. *J. Chem. Phys.* **2010**, *132*, 154104. [CrossRef]
36. Grimme, S.; Ehrlich, S.; Goerigk, L. Effect of the damping function in dispersion corrected density functional theory. *J. Comput. Chem.* **2011**, *32*, 1456–1465. [CrossRef] [PubMed]
37. Kruse, H.; Grimme, S. A geometrical correction for the inter-and intra-molecular basis set superposition error in Hartree-Fock and density functional theory calculations for large systems. *J. Chem. Phys.* **2012**, *136*, 04B613. [CrossRef]
38. Lefebvre, C.; Rubez, G.; Khartabil, H.; Boisson, J.C.; Contreras-García, J.; Hénon, E. Accurately extracting the signature of intermolecular interactions present in the NCI plot of the reduced density gradient versus electron density. *Phys. Chem. Chem. Phys.* **2017**, *19*, 17928–17936. [CrossRef]
39. Lu, T.; Chen, F. Multiwfn: A multifunctional wavefunction analyzer. *J. Comput. Chem.* **2012**, *33*, 580–592. [CrossRef] [PubMed]
40. Neese, F. The ORCA program system. *Wiley Interdiscip. Rev. Comput. Mol. Sci.* **2012**, *2*, 73–78. [CrossRef]
41. Neese, F. Software update: The ORCA program system—Version 5.0. *Wiley Interdiscip. Rev. Comput. Mol. Sci.* **2022**, *12*, e1606. [CrossRef]
42. Humphrey, W.; Dalke, A.; Schulten, K. VMD: Visual molecular dynamics. *J. Mol. Graph.* **1996**, *14*, 33–38. [CrossRef] [PubMed]
43. Amrhar, O.; El Gana, L.; Mobarak, M. Calculation of adsorption isotherms by statistical physics models: A review. *Environ. Chem. Lett.* **2021**, *19*, 5419–5447. [CrossRef]
44. Tran, H.N.; You, S.J.; Chao, H.P. Effect of pyrolysis temperatures and times on the adsorption of cadmium onto orange peel derived biochar. *Waste Manag. Res.* **2016**, *34*, 129–138. [CrossRef]
45. Yang, Z.; Liu, X.; Zhang, M.; Liu, L.; Xu, X.; Xian, J.; Cheng, Z. Effect of temperature and duration of pyrolysis on spent tea leaves biochar: Physiochemical properties and Cd(II) adsorption capacity. *Water Sci. Technol.* **2021**, *154*, 105010. [CrossRef]
46. Chen, D.; Cen, K.; Zhuang, X.; Gan, Z.; Zhou, J.; Zhang, Y.; Zhang, H. Insight into biomass pyrolysis mechanism based on cellulose, hemicellulose, and lignin: Evolution of volatiles and kinetics, elucidation of reaction pathways, and characterization of gas, biochar and bio-oil. *Combust. Flame* **2022**, *242*, 112142. [CrossRef]
47. Sánchez, F.; Araus, K.; Domínguez, M.P.; Miguel, G.S. Thermochemical transformation of residual avocado seeds: Torrefaction and carbonization. *Waste Biomass Valorization* **2017**, *8*, 2495–2510. [CrossRef]
48. Hoinacki, C.K.; Polidoro, A.S.; Cabrera, P.M.; Thue, P.S.; Assis, R.; Lima, E.C.; Bussamara, R.; Fernandes, A.N. Laccase covalently immobilized on avocado seed biochar: A high-performance biocatalyst for acetaminophen sorption and biotransformation. *J. Environ. Chem. Eng.* **2022**, *10*, 107731. [CrossRef]
49. Kopac, T.; Toprak, A. Hydrogen sorption characteristics of Zonguldak region coal activated by physical and chemical methods. *Korean J. Chem. Eng.* **2009**, *26*, 1700–1705. [CrossRef]
50. Peng, Z.; Xu, Y.; Luo, W.; Wang, C.; Ma, L. Conversion of biomass wastes into activated carbons by chemical activation for hydrogen storage. *ChemistrySelect* **2020**, *5*, 11221–11228. [CrossRef]
51. Purkayastha, S.K.; Guha, A.K. H_2 and CO_2 adsorption ability of cationic lithiated carbenes: A computational study. *Int. J. Hydrogen Energy* **2022**, *47*, 39917–39930. [CrossRef]

52. Ma, L.; Li, J.; Ma, X. Preparation and adsorption of CO_2 and H_2 by activated carbon hollow fibers from rubber wood (*Hevea brassiliensis*). *BioResources* **2019**, *14*, 9755–9756.
53. Schaefer, S.; Jeder, A.; Sdanghi, G.; Gadonneix, P.; Abdedayem, A.; Izquierdo, M.T.; Maranzana, G.; Ouederni, A.; Celzard, A.; Fierro, V. Oxygen-promoted hydrogen adsorption on activated and hybrid carbon materials. *Int. J. Hydrogen Energy* **2020**, *45*, 30767–30782. [CrossRef]
54. Hegde, S.S.; Bhat, B.R. Biomass waste-derived porous graphitic carbon for high-performance supercapacitors. *J. Energy Storage* **2024**, *76*, 109818. [CrossRef]
55. Anoop, P.P.; Palanisamy, T. Coconut shell biochar–*Bacillus cereus* DKBovi-5 based biocomposite as a sustainable additive for cement mortar: Effect of pyrolysis temperature on characterization, strength, hydration, and healing. *Sustain. Chem. Pharm.* **2025**, *46*, 102112. [CrossRef]
56. Liu, B.; Ma, X.; Shi, R.; Zhou, K.; Xu, X.; Qiu, J.; Wang, H.; Zeng, Z.; Li, L. Synthesis of alkali metals functionalized porous carbon for enhanced selective adsorption of carbon dioxide: A theoretically guided study. *Energy Fuels* **2021**, *35*, 15962–15968. [CrossRef]
57. Cho, S.; Lyu, L.; Kang, Y.M. Electrochemical role of Li-ligands at the triple-phase boundary in Li-O_2 batteries. *ACS Appl. Mater. Interfaces* **2025**, *17*, 32141–32149.
58. Ma, J.; Nan, H.; Yang, G.; Li, Z.; Wang, J.; Zhou, J.; Xue, C.; Wang, X.; Xu, S. Lithium-functionalized TEMPO-oxidized cellulose nanofiber as a novel binder and its impact on the ionic conductivity performance of lithium-ion batteries. *Cellulose* **2024**, *31*, 9681–9698.
59. Bediako, J.K. Effects of carbon precursors and activation agents on the physicochemical characteristics and aurocyanide adsorption patterns of agro waste-based activated carbons. *Results Eng.* **2026**, *29*, 108715.
60. Guerra-Que, Z.; López-Margalli, K.S.; Urrieta-Saltijeral, J.M.; Silahua-Pavón, A.A.; Martínez-García, H.; García-Alamilla, P.; Córdova-Pérez, G.E.; Arévalo-Pérez, J.C.; Torres-Torres, J.G. Activated carbon synthesised from lignocellulosic cocoa pod husk via alkaline and acid treatment for methylene blue adsorption: Optimisation by response surface methodology, kinetics, and isotherm modelling. *RSC Adv.* **2025**, *15*, 47231–47254. [CrossRef]
61. Saraugi, S.S.; Asare, F.; Gazo, R.; Mohanta, T.R.; Saha, P.; Routray, W. A comprehensive characterization of tender coconut waste biochar produced through slow pyrolysis at different temperatures and heating rates. *Biomass Bioenergy* **2026**, *207*, 108728.
62. Handiso, B.; Pääkkönen, T.; Wilson, B.P. Effect of pyrolysis temperature on the physical and chemical characteristics of pine wood biochar. *Waste Manag. Bull.* **2024**, *2*, 281–287. [CrossRef]
63. Jerigová, M.; Odziomek, M.; López-Salas, N. "We are here!" Oxygen functional groups in carbons for electrochemical applications. *ACS Omega* **2022**, *7*, 11544–11554. [CrossRef]
64. Alfarra, A.; Frackowiak, E.; Béguin, F. Mechanism of lithium electrosorption by activated carbons. *Electrochim. Acta* **2002**, *47*, 1545–1553. [CrossRef]
65. Ren, P.; Ji, P. Polyacrylic acid-grafted alkali-activated fly ash as a novel adsorbent for Lithium recovery: Unraveling adsorption performance and underlying mechanisms. *J. Mol. Liq.* **2025**, *438*, 128709. [CrossRef]
66. Lu, Y.; Zhang, Z.; Zhong, Q.; Yao, Z.; Wu, J.; Zhang, J.; Wang, L.; Xiao, J. Oxygen-rich modified-graphite recycled from spent lithium batteries for improved lithium-ion storage: Adsorption and intercalation mechanisms. *Sep. Purif. Technol.* **2025**, *359*, 130798. [CrossRef]
67. An, Y.; Sun, Y.; Zhang, K.; Li, C.; Sun, X.; Wang, K.; Zhang, X.; Ma, Y. Tuning surface functional groups and crystallinity in activated carbon for high-voltage lithium-ion capacitors. *New Carbon Mater.* **2025**, *40*, 1085–1097. [CrossRef]
68. Lin, X.; Wu, J.; Lin, J.; Wang, N.; Su, M.; Tang, J.; Shih, K.; Xu, J. Selective recovery of Ni, Co, and Li from spent NCA lithium-ion batteries: 3D macroporous bio-based adsorbent and innovative leaching–adsorption strategy. *J. Environ. Chem. Eng.* **2025**, *13*, 118063. [CrossRef]
69. Malini, K.; Selvakumar, D.; Kumar, N.S. Activated carbon from biomass: Preparation factors improving basicity and surface properties for enhanced CO_2 capture capacity—A review. *J. CO_2 Util.* **2023**, *67*, 102318. [CrossRef]
70. Kim, J.H.; Lee, G.; Park, J.E.; Kim, S.H. Limitation of K_2CO_3 as a chemical agent for upgrading activated carbon. *Processes* **2021**, *9*, 1000. [CrossRef]
71. Chen, C.; Zhang, J.; Zhang, B.; Duan, H.M. Hydrogen adsorption of Mg-doped graphene oxide: A first-principles study. *J. Phys. Chem. C* **2013**, *117*, 4337–4344. [CrossRef]
72. Li, Z.; Xu, Z.; Gao, C. Selective proximate antarafacial distribution of oxidized functional groups on graphene oxide. *J. Phys. Chem. C* **2024**, *128*, 1323–1331. [CrossRef]
73. Mofidi, F.; Reisi-Vanani, A. Investigation of the electronic and structural properties of graphyne oxide toward CO, CO_2 and NH_3 adsorption: A DFT and MD study. *Appl. Surf. Sci.* **2020**, *507*, 145134. [CrossRef]
74. Ayesh, A.I. Investigation of BN modified graphene nanoribbon for gas adsorption applications: DFT study. *Chin. J. Phys.* **2023**, *85*, 649–659. [CrossRef]
75. Yang, L.; Sun, L.; Deng, W.Q. van der Waals function for molecular mechanics. *J. Phys. Chem. A* **2020**, *124*, 2102–2107. [CrossRef]

76. Zhou, Y.; Chu, W.; Jing, F.; Zheng, J.; Sun, W.; Xue, Y. Enhanced hydrogen storage on Li-doped defective graphene with B substitution: A DFT study. *Appl. Surf. Sci.* **2017**, *410*, 166–176. [CrossRef]
77. Shen, D.; Liu, Z.; Tu, Z.; Li, S. Understanding hydrogen adsorption performance of lithium-doped MIL-101 (Cr) by molecular simulations: Effects of lithium distribution. *Int. J. Hydrogen Energy* **2023**, *48*, 18366–18374. [CrossRef]
78. Srinivasu, K.; Ghosh, S.K. Theoretical studies on hydrogen adsorption properties of lithium decorated diborene ($B_2H_4Li_2$) and diboryne ($B_2H_2Li_2$). *Int. J. Hydrogen Energy* **2011**, *36*, 15681–15688.
79. Bi, L.; Yin, J.; Huang, X.; Wang, Y.; Yang, Z. A DFT study of H_2 adsorption on lithium decorated 3D hybrid Boron-Nitride-Carbon frameworks. *Int. J. Hydrogen Energy* **2019**, *44*, 15183–15192.
80. Johnson, E.R.; Keinan, S.; Mori-Sánchez, P.; Contreras-García, J.; Cohen, A.J.; Yang, W. Revealing noncovalent interactions. *J. Am. Chem. Soc.* **2010**, *132*, 6498–6506. [CrossRef]
81. Wen, Y.; Chai, X.; Gu, Y.; Wu, W.; Ma, W.; Zhang, J.; Zhang, T. Advances in hydrogen storage materials for physical H_2 adsorption. *Int. J. Hydrogen Energy* **2025**, *97*, 1261–1274. [CrossRef]